Electronic Supplementary Information

Natural Skin-inspired Cellulose Versatile Biomimetic Hydrogels

Fengcai Lin [a], Zi Wang [a], Yanping Shen [a], Lirong Tang [a], Pinle Zhang [a], Yuefang Wang [a], Yandan Chen [a], Biao Huang *[a], Beili Lu*[a]

[a] College of Material Engineering, Fujian Agriculture and Forestry University, Fuzhou 350108, China.

*E-mail: lubl@fafu.edu.cn; bhuang@fafu.edu.cn

Experimental Section

Materials: Bleached bamboo pulp (α-cellulose content > 95%) was provided by Nanping Paper Co., Ltd. (Nanping, Fujian, China). The weight average molecular weight (M_w) and the number average molecular weight (M_n) of bamboo cellulose pulp were 203 000 and 58 000, respectively. Tannic acid, silver nitrate ($AgNO_3$, over 99.0% purity), tris(hydroxymethyl)aminomethane (Tris), poly(vinyl alcohol) (PVA, DS=1750 ± 50, M_w=75,000-80,000 g/mol, over 99.0% purity) and sulfuric acid (H_2SO_4, over 99.0% purity) were purchased from Sinopharm Chemical Reagent Co., Ltd. (Beijing, China). Borax (sodium tetraborate decahydrate, over 99.5% purity, $Na_2B_4O_7 \cdot 10H_2O$, M_w = 381.37 g/mol) was obtained from Aladdin Industrial Corporation (Shanghai, China). All the chemicals were used without further purification, and distilled water was used for the preparation of aqueous solutions.

Extraction of Cellulose Nanocrystals (CNC): Cellulose nanocrystals (CNC) was extracted from bleached bamboo cellulose pulp by acid hydrolysis assisted with ultrasonication as described in our previous literature[1]. 5.0g of bamboo pulp was hydrolyzed with 55 wt% H_2SO_4 solution (250mL) at 60℃ under ultrasonic treatment with vigorous stirring for 90 min. The resulting suspension was washed with distilled water in centrifugation until neutrality, and then the CNC suspension was collected through a sequence of repeated centrifugation at 5000 rpm. The obtained CNC suspension was then dialyzed against distilled water for 7 days and then concentrated to 1.5 wt % before use.

Synthesis of Ag/TA@CNC Nanocomplexes: The Ag/TA@CNC nanocomplexes were synthesized via a two-step process (as shown in Figure 1). In the first step, 134.0 g CNC

suspension (1.5 wt%, containing about 2.0 g CNC) was diluted to 500 mL with distilled water, and Tris buffer solution (1 M) was dropwise added into the CNC suspension to adjust the pH to 8.5. Then, 2.0 g tannic acid was introduced and magnetically stirred at room temperature for 12 h. After reaction, the products (labeled as TA@CNC) were purified by repeated centrifugation and redispersed in distilled water (3.0 wt%). For the second step, 5.0 g of $AgNO_3$ was dissolved in the 1000 mL distilled water, and ammonia solution (5.0 wt%) was dropwise added until the solution became clear, confirming the formation of diamine silver (I). Subsequently, 50.0 g of TA@CNC suspension (3.0 wt%) was introduced and the resultant solution was stirred at room temperature for 6 h. Finally, the products (labeled as Ag/TA@CNC) were collected by centrifugation at 9000 rpm, and washed three times with distilled water. The synthesized Ag/TA@CNC nanocomplexes were redispersed in distilled water with ultrasonic treatment to form the homogeneous suspension with concentration of 6.0 wt% and stored for further use.

Preparation of PB-Ag/TA@CNC Hybrid Hydrogels: The nanocomposite hydrogels with 1.0 wt% of Ag/TA@CNC nanocomplexes, 10.0 wt% of PVA and 0.6 wt% of borax were prepared as follows. First, 10.0 g PVA and 16.7 g Ag/TA@CNC suspension (6.0 wt%) was dissolved in 68.3 mL distilled water with continuous stirring at 95℃ until the PVA was completely dissolved. Then, 0.6 g borax was dissolved in 4.4 mL of distilled water and added to the above solution. The mixture was stirred vigorously until the homogenous solution with well dispersed Ag/TA@CNC was formed. As the temperature slowly decreased, the mixture started to exhibit viscoelasticity. When the solution was further cooled to ambient temperature, homogeneously stable hybrid hydrogels were finally formed. A series of nanocomposite

hydrogels with 0.0 wt%, 1.0 wt%, 2.0 wt%, 3.0 wt%, 4.0 wt%, and 5.0 wt% of Ag/TA@CNC nanocomplexes were labeled as PB-Ag/TA@CNC0, PB-Ag/TA@CNC1, PB-Ag/TA@CNC2, PB-Ag/TA@CNC3, PB-Ag/TA@CNC4, and PB-Ag/TA@CNC5, respectively. As a control, the PVA-borax hydrogel with 4.0 wt% of pure CNC was also prepared with the above method and designated as PB-CNC4.

Characterization of PB-Ag/TA@CNC Hydrogels: The morphology of cellulose nanocrystals were carried out on a Hitachi H-7650 (Japan) electron microscope at an acceleration voltage of 80 kV. The microstructure of the PB-Ag/TA@CNC hydrogels was observed by scanning electron microscope (SEM, SU8010, Hitachi, Japan) at an acceleration voltage of 40 kV. Before observation, hydrogel samples were freeze-dried and coated with gold. FTIR spectra of the samples in KBr discs were performed on a NICOLET 380 FTIR spectrometer (Thermo Electron Instruments Co., Ltd., USA) in the range of 400-4000 cm^{-1} with 32 scans. X-ray photoelectron spectroscopy (Thermo Electron corporation, USA) was conducted with monochromatic Al Kα radiation (1254.0 eV). Spectra were recorded over a range of 0-1300eV, followed by high resolution scan of the O1s and C1s regions.

Rheological Measurement: Rheological behaviors of PB-Ag/TA@CNC hydrogels were analyzed with a rheometer Rotational Rheometer MARS III Haake (Thermo Scientific, Germany) equipped with a parallel plate geometry (35 mm in diameter). Oscillatory frequency sweeps (strain=10%) was conducted from 0.01 to 10 Hz at 25 °C. Recovery rests were carried out by straining sample to failure with increasing sweep strain from 0.1-1000%, and then suing time sweep module to record the recovery of storage modulus (G') and loss modulus (G'') as a function of time. Moreover, the G' and G'' dependence of time in continuous step strain for

PB-Ag/TA@CNC hydrogels were carried out with the change of amplitude oscillatory force from strain of 1% to 200% under the same frequency of 1.0 Hz.

Mechanical Performance Tests: The mechanical properties of the PB-Ag/TA@CNC hydrogels were carried out on a universal testing machine (ETM520C, WANCE, China). Five rectangular specimens with the size of 10 cm × 1 cm × 0.3 cm were prepared, and the tensile test were performed with a constant stretching rate of 100 mm/min. For self-healing experiment, the samples (10 cm × 1 cm × 0.3 cm) were cut into halves, and then the two pieces of hydrogels were brought into contact at room temperature. After self-healing for 10 min, the tensile test were carried out to quantitatively evaluate the self-healing properties of the PB-Ag/TA@CNC hydrogels.

Adhesion Measurement: The adhesive strengths of the PB-Ag/TA@CNC hydrogels on a variety of substrates, including wood, glass, plastic, steel, and porcine skin, were investigated via a lap shear testing method. The substrates were cut into 20 mm × 20 mm squares and attached to steel plates (20 mm × 50 mm × 2mm) by using cyanoacrylate glue. Then, a PB-Ag/TA@CNC hydrogel with 20 mm × 20 mm × 1mm was placed between two substrates and compressed with a 100 g weight for 5 min. Next, the adhered plates were pulled to separation at a speed of 10 mm/mim on the universal testing machine. The adhesion strength was calculated by the measured maximum load divided by the adhesive areas.

Electrical Behavior Measurements: The electrical conductivity of the PB-Ag/TA@CNC hydrogels were determined by a four point probe measurements (HS-MPRT-4) at room temperature. To determine the resistance variation during stretching, the samples were fixed on a universal testing machine with a stretching rate of 100 mm/min and the resistance value

were recorded by LCR meter (TH2830) at an AC voltage of 1 V and a sweeping frequency of 1 kHz.

Hydrogel Based Flexible Sensor Fabrication: A capacitance sensor was constructed by integrating two PB-Ag/TA@CNC4 hydrogel layers with a dielectric layer (Very High Bond tape (VHB) 4905, 3M), and linked with two metallic electrodes. Additional two layers of VHB were used to wrap the whole sensor to protect the sensor and prevent the water evaporation. Capacitance measurements were recorded by an LCR meter (TH2830) at an AC voltage of 1 V and a sweeping frequency of 1 kHz to detect various external mechanical stimuli on the sensor device.

Antibacterial Performance Tests: The antibacterial performance of PB-Ag/TA@CNC hydrogels were evaluated by *Escherichia coli* (*E. coli*) and *Staphylococcus aureus* (*S. aureus*) as Gram-negative and Gram-positive bacteria models via inhibition zone method. The hydrogels were cut into disks with a diameter of 23 mm, and then exposed to UV light for 60 min per side. 100 μL of *E. coli* or *S. aureus* in broth (10^5 CFU/mL) was dispersed onto the agar culture medium respectively. Next, the hydrogel disks were carefully placed onto the surface of the agar plate and incubated for 24 h at 37℃. After incubation, the inhibition halos around the samples were observed and their diameters were measured.

Supporting Tables and Figures

Table S1. Mechanical properties of PB-Ag/TA@CNC hydrogels

Samples	Fracture strain (%)	Fracture strength (kPa)	Elastic modulus (kPa)	Toughness (MJ/m^3)
PB-Ag/TA@CNC0	1747.7	49.8	211.8	0.9
PB-Ag/TA@CNC1	2568.4	130.9	261.6	2.9
PB-Ag/TA@CNC2	3383.2	180.4	299.2	5.2
PB-Ag/TA@CNC3	3809.2	214.3	324.88	7.3
PB-Ag/TA@CNC4	4106.4	246.1	346.52	9.4
PB-Ag/TA@CNC5	4015.7	229.3	465.56	8.8
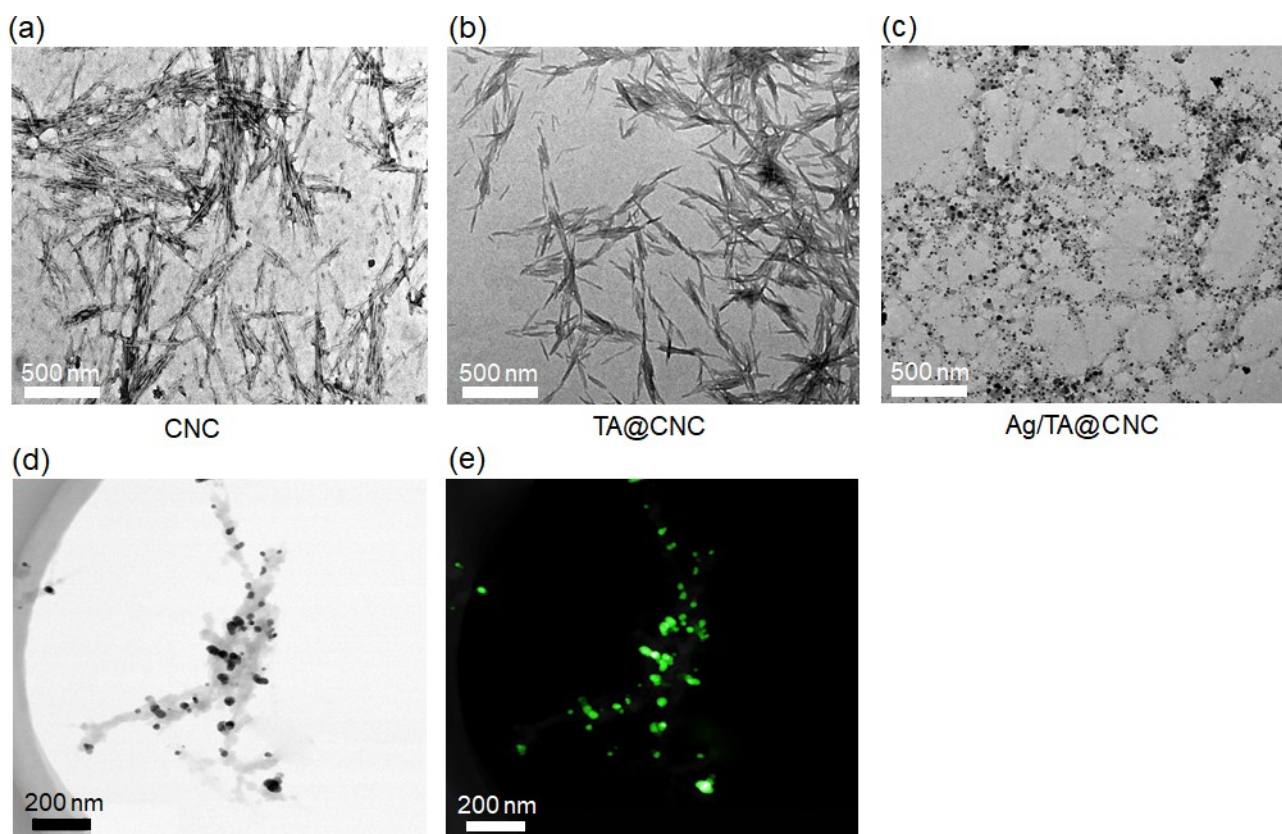
Figure S1. TEM images of pristine CNC (a), core-shell TA@CNC (b) and Ag/TA@CNC (c, d). The corresponding EDS mapping obtained from Figure S1d (e).

The TEM images in Figure S1a-crecorded the morphologies evolution from well-dispersed CNC to TA coated CNC (TA@CNC) and Ag/TA@CNC nanocomplexes. As shown in Figure S1a, CNC exhibited a rod-like structure with 25-50 nm in diameter and 200-500 nm in length. After assembly coating process, a flocculent TA layer was coated on CNC in TA@CNC nanohybrid, which exhibited a remarkably thickened wall (Figure S1b). After treating TA@CNC with diammine silver (I) solution, a densely and uniformly distributed sliver nanoparticles (20~30 nm) can be clearly observed on the surface of Ag/TA@CNC nanocomplexes (Figure S1c), indicating the successful deposition of Ag nanoparticles onto the surface of TA@CNC. Moreover, the morphology and distribution of Ag nanoparticles on the surface of TA@CNC can also be obviously evidenced by EDS silver elemental mapping analysis (Figure S1d-e).
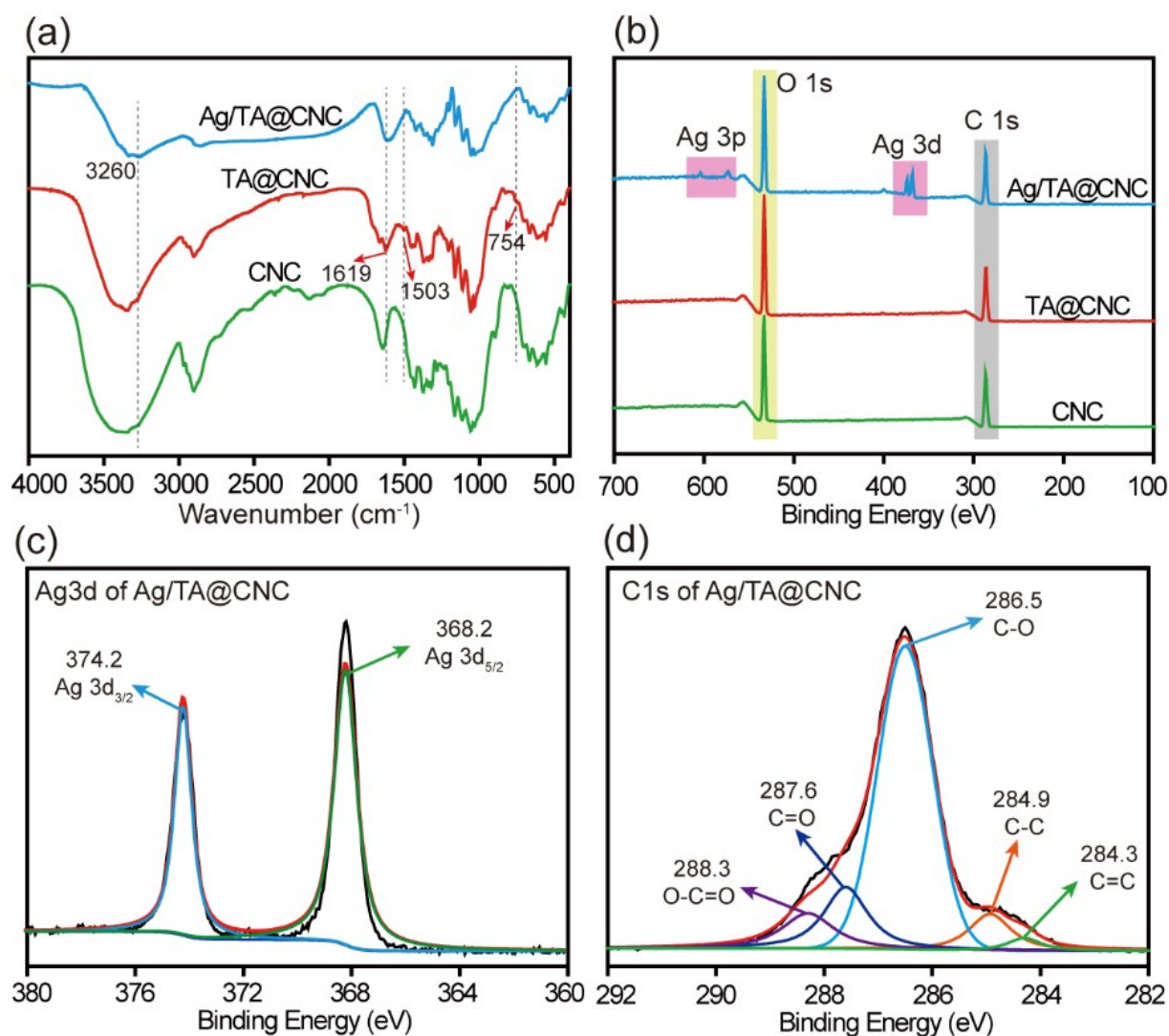
Figure S2. (a) FTIR spectra and XPS wide-scan (b) of CNC, TA@CNC and Ag/TA@CNC. (c) Ag 3d XPS spectrum of Ag/TA@CNC. (d) C1s high-resolution XPS spectrum of Ag/TA@CNC.

FTIR and XPS were used to identify the successful surface modification of CNC (Figure S2). As displayed in Figure S2a, after coating with TA, the specific peaks of CNC were relatively well-retained and some notable stretching peaks at 1619 cm^{-1}, 1503 cm^{-1} and 754 cm^{-1} appeared, indicating aromatic C-C stretching vibrations and typical peaks of C=C distortion vibration from benzene rings in the TA@CNC[2]. By further in situ growing Ag nanoparticles on TA@CNC, the intensity of the major peaks decreased significantly together with a read shift and broaden of the absorption peak at ~ 3260 cm^{-1}. XPS spectroscopy was utilized to further analyze the element composition changes of

nanohybrid at each step of the modification. As shown in Figure S2b, the XPS spectra of original and TA-coated CNC exhibited only C1s at ~286 eV and O1s peak at ~533 eV. In contrast, some notable peaks at ~590 eV and ~370 eV appeared for the spectra of Ag/TA@CNC due to the presence of Ag nanoparticles and their aggregates[3]. Moreover, a spin energy separation of 6.0 eV between Ag $3d_{5/2}$ and Ag $3d_{3/2}$ was observed in Figure S2c, which corresponding to the metallic sliver (Ag^0) on the CNC surface[4]. In addition, as shown in the high-resolution C1s spectrum of Ag/TA@CNC (Figure S2d), the TA coating layer can be revealed by different chemical states of C elemental containing C=C (284.3 eV), C-C (284.9 eV), C-O (286.5 eV), C=O (287.6 eV), and O-C=O (288.3 eV)[3, 5]. Taken together, these results indicated that the multifunctional TA layer and Ag nanoparticles were successfully bonded onto the surface of CNC.
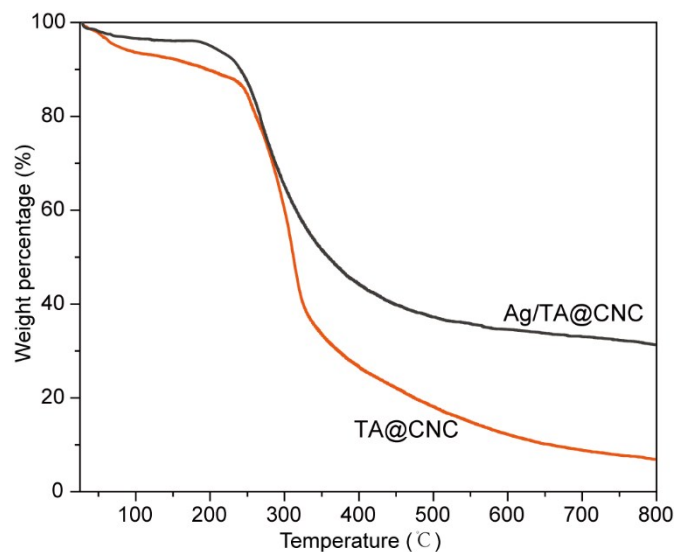
Figure S3. TG curves of TA@CNC, and Ag/TA@CNC.

The content of Ag nanoparticles could be calculated based on the TG curves of TA@CNC and Ag/TA@CNC (Figure S3). As shown in Figure S3, a significant weight loss of TA@CNC was observed after 250 ℃ due to the continue decomposition of the carbon skeleton. And the weight loss of TA@CNC was up to 95.47% at 800 ℃. After introducing Ag nanoparticles, the decomposition of Ag/TA@CNC became slower because of the interactions between Ag nanoparticles and TA@CNC. At 800 ℃, the residue was 24.48% for Ag/TA@CNC. Thus, the content of Ag nanoparticles can be calculated to be 19.95%.
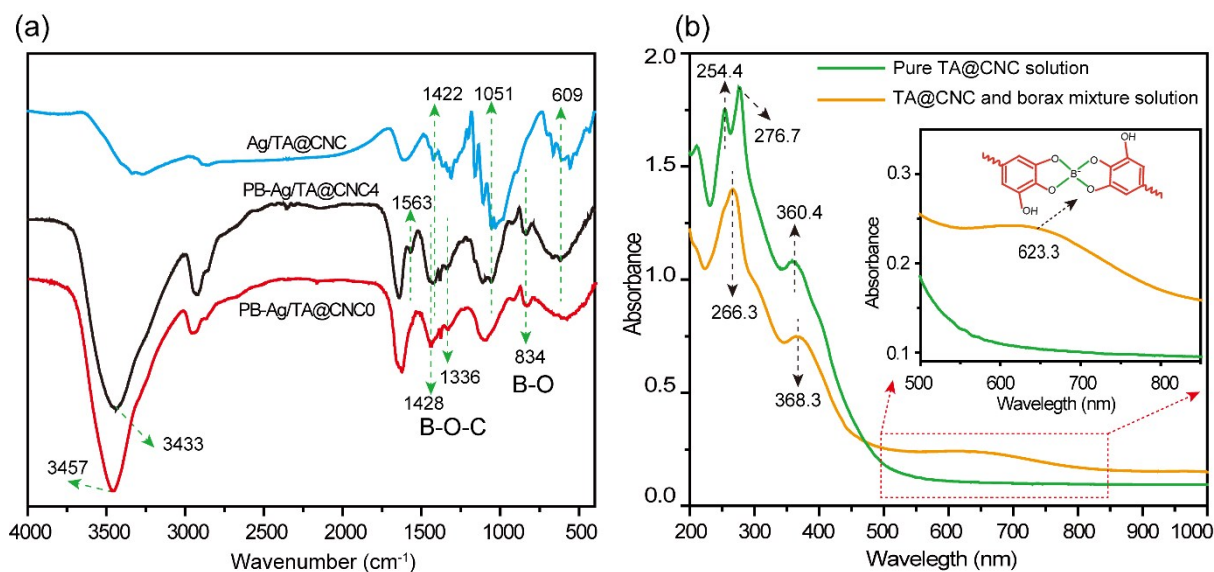
Figure S4. (a) FTIR spectra of Ag/TA@CNC, PB-Ag/TA@CNC0, and PB-Ag/TA@CNC4. (b) UV-vis spectra of pure TA@CNC solution and TA@CNC-borax mixture solution (with TA@CNC: borax ratios of 5:1).

As shown in Figure S4a, for PB-Ag/TA@CNC4, the broad, large band at 3433 cm^{-1} was attributed to the O-H stretching and involved in intermolecular hydrogen boding[6]. After introducing the Ag/TA@CNC, the pronounced redshifts of -OH group vibration (from 3457 cm^{-1} of PB-Ag/TA@CNC0 to 3433 cm^{-1} of PB-Ag/TA@CNC4) indicated the formation of intensity hydrogen boding between Ag/TA@CNC and matrix[7]. The feature absorption peaks at 1563 cm^{-1} (C=C distortion vibration from benzene rings of TA), 1422 cm^{-1} (CH$_2$ shearing vibration), 1051 cm^{-1} (C-O stretching vibration), and 609 cm^{-1} (C-C stretching vibration) confirm the existence of Ag/TA@CNC in the PB-Ag/TA@CNC4 hydrogel. Moreover, the hydrogels displayed several characteristic peaks of borax and borate, including 1428 cm^{-1} and 1334 cm^{-1} (asymmetric stretching relaxation of B-O-C), 834 cm^{-1} (B-O stretching from residual B(OH)$_4^-$), demonstrating the multi-complexation and crosslinking between Ag/TA@CNC nanohybrid, PVA chains, and borate[8, 9]. Moreover, UV-vis spectroscopy was used to further confirm the catechol-borate bonds. As shown in Figure S4b, for the

spectra of pure TA@CNC, the absorption peaks appeared at 254.4 and 276.7 nm due to the absorption of the catechol groups from TA[10]. An absorbance peak located at 360.4 nm ascribe to the formation of quinone, which was consistent with the proposed reaction process of the oxidation of catechol groups into quinone during the TA coating procedure[11, 12]. However, after mixing with borax solution (with TA@CNC : borax ratios of 5:1), the UV-vis spectra revealed a large absorption peak at around 623.3 nm resulting from covalent catechol-borate bonds, and simultaneous disappeared peak at 254.4 nm attributed to free catechol groups, further indicating the formation of complexation between catechol and borax[13-16].
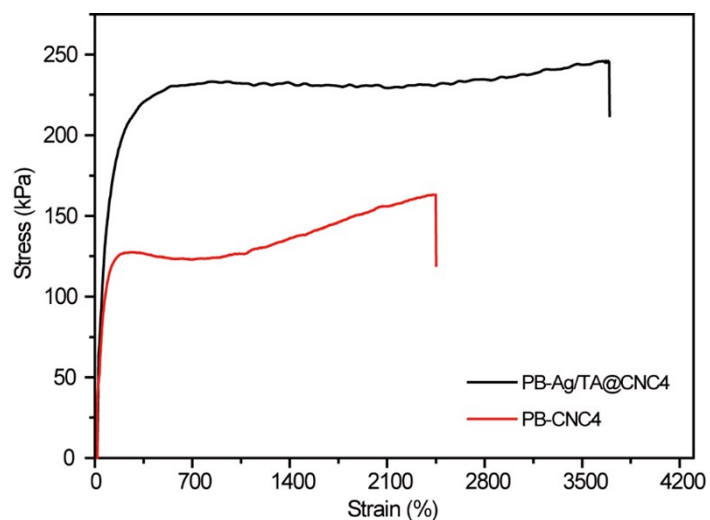
Figure S5. Tensile stress-strain curves of PB-Ag/TA@CNC4 hydrogel and PB-CNC4 hydrogel (reinforced with 4.0% CNC).
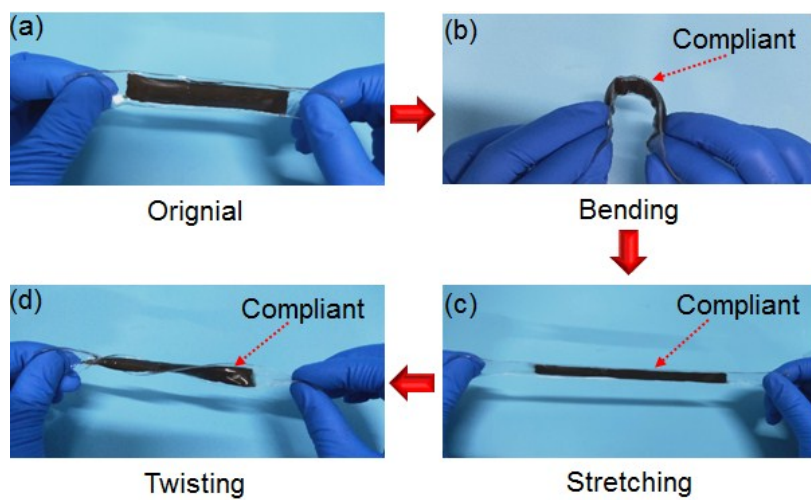
Figure S6. The PB-Ag/TA@CNC4 hydrogel is compliant when being bended, stretched and twisted.
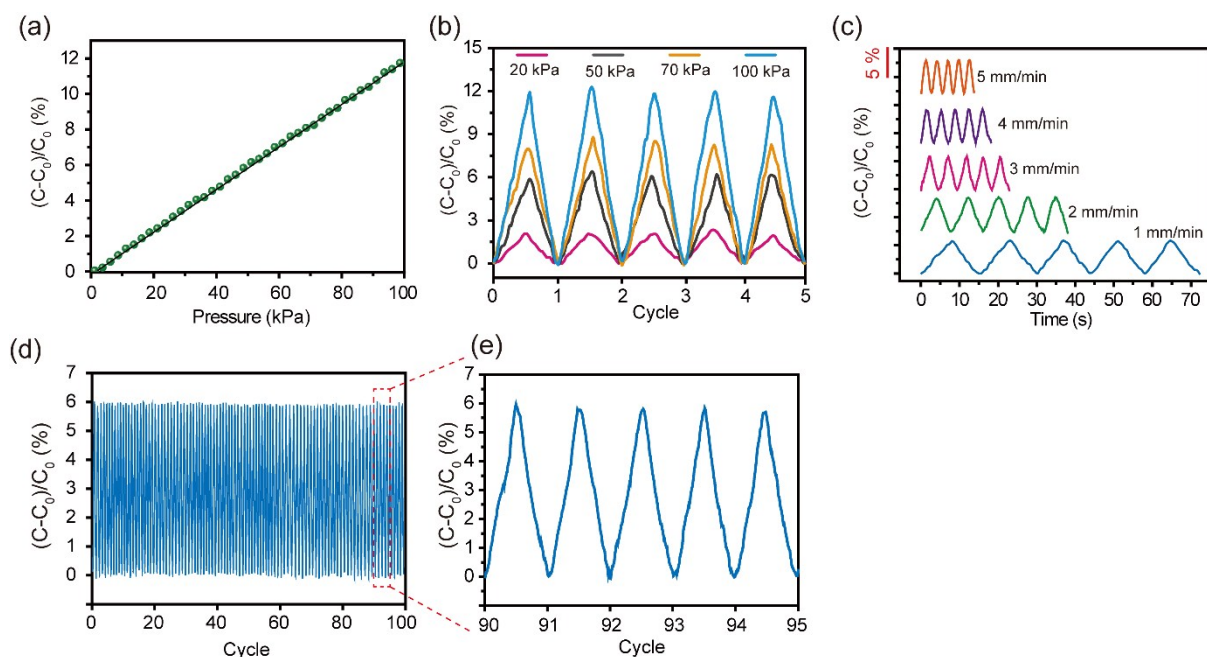
Figure S7. (a) Relative capacitance variations versus pressure for the hydrogel sensor. (b) Relative capacitance changes under different cyclic loading-unloading stress. (c) Relative capacitance variations at a pressure of 50 kPa with different applied speeds of 1 mm/min, 2 mm/min, 3 mm/min, 4 mm/min, 5 mm/min, respectively. (d) Responsive stability of the PB-Ag/TA@CNC4 hydrogel capacitance sensor under repeatedly loading-unloading at a pressure of 50 kPa for 100 cycles. (e) Magnified signal during 90-95 cycles.

As shown in Figure S7a, the device also displays a clear linearly capacitance responsive as a function of compressive pressure from 0 to 100 kPa. Figure S7b depicts the capacitance variation curve under different pressure. Larger pressure can generate more remarkable change in efficiency area of the conductive layer, resulting in a more obvious capacitance variation. As shown in Figure S7c, the capacitance change amplitude of the sensor device displays almost no frequency dependence in certain stress (50kPa), which is crucial to the sensor's practical application. Moreover, the stable and reproducible response was also confirmed by repeated loaded/unloaded pressure with 50 kPa for 100 times (Figure S7d-e).
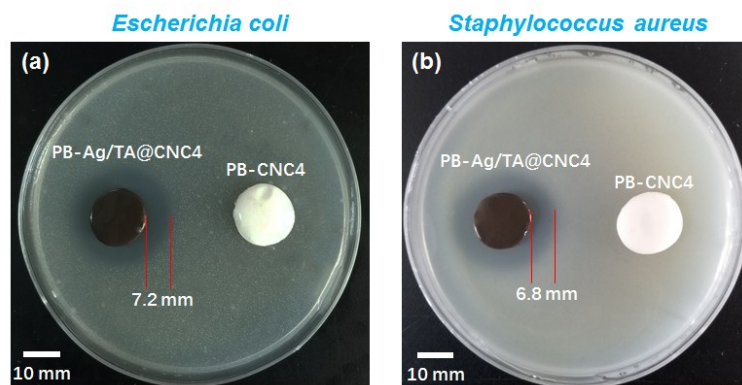
Figure S8. Antimicrobial activities of PB-Ag/TA@CNC4 hydrogel and PB-CNC4 hydrogel (reinforced with 4.0% CNC) evaluated against Gram-negative viz *Escherichia coli* (*E. coli*) (a) and Gram-positive viz *Staphylococcus aureus* (*S. aureus*) (b).

Table S2. Comparison of reported skin-like materials with this work in functionalities mimicking

Components for skin-like materials	Healing condition	Healing efficiency	Conformability	Stretchability	Self-adhesiveness	Antimicrobial	Sensibility	Ref.
Ag/TA@CNC /borax/ PVA	RT	10 min for 98.6% healing efficiency	Yes	~4100%	Yes	Yes	Yes	**This work**
ACC / PAA /alginate	RT	—	Yes	~1000%	—	—	Yes	[17]
PANI/ PAA/ PA	60% humidity	24h for 99% healing efficiency	—	~500%	—	—	Yes	[18]
PAAM/ NaCl/EG/PLA	—	—	Yes	~1700%	—	—	Yes	[19]
Aa/Ta/HMA/PAAM	—	—	—	~2100%	Yes	—	Yes	[20]
PDA@Ag/PANI/PVA,	RT	2h for 97% healing efficiency	—	—	Yes	Yes	Yes	[21]
PAA/PVA/Fe^{3+}/ borax/CNT/EG	RT	6h for 90.4% healing efficiency	—	~550%	—	—	Yes	[22]
PAM/Au@PDA GW	37 ℃	24h for 63% healing efficiency	—	~900%	Yes	—	Yes	[23]
PVA/GE/GL/NaCl	—	—	—	~715%	—	—	Yes	[24]
PVA/Silk fibroin/Borax	RT	—	—	~5000%	Yes	—	Yes	[25]
PAM/MWCNTs	Keep wet	24h	—	~2000%	—	—	Yes	[26]
NaCl/SA/PAM	RT	—	—	~3100%	—	—	Yes	[27]
PAA/GO/Ca^{2+}	RT	20h for 88.4% healing efficiency	Yes	~2500%	—	—	Yes	[28]
Ag flakes/ Ecoflex	—	—	Yes	~1780%	—	—	Yes	[29]
PAA/CS/PPy/Fe^{3+}	RT	2min for 100% healing efficiency	Yes	~1500%	—	—	Yes	[30]
TiO_2-CD/CS/PVA	—	—	Yes	~278%	Yes	—	Yes	[31]

"RT": room temperature;

"—": not available in the references

References

1   Q. Lu, L. Tang, S. Wang, B. Huang, Y. Chen and X. Chen, *Biomass Bioenergy*, 2014, **70**, 267-272.

2   Z. Hu, R. M. Berry, R. Pelton and E. D. Cranston, *ACS Sustainable Chem. Eng.*, 2017, **5**, 5018-5026.

3   Y. Bu, S. Zhang, Y. Cai, Y. Yang, S. Ma, J. Huang, H. Yang, D. Ye, Y. Zhou and W. Xu, *Cellulose*, 2019, **26**, 2109-2122.

4   Z. Wei, G. Li, L. Wang, Z. Chen and Y. Lin, *Appl. Surf. Sci.*, 2017, **413**, 140-148.

5   W. Zhong, H. Kang, Z. Wei, S. Zhang and J. Li, *Appl. Surf. Sci.*, 2017, **401**, 271-282.

6   U. Manna and S. Patil, *J. Phys. Chem. B*, 2009, **113**, 9137-9142.

7   Y. Chen, L. Peng, T. Liu, Y. Wang, S. Shi and H. Wang, *ACS Appl. Mater. Interfaces*, 2016, **8**, 27199-27206.

8   O. Koysuren, M. Karaman and H. Dinc, *J. Appl. Polym. Sci.*, 2012, **124**, 2736-2741.

9   S. Spoljaric, A. Salminen, N. D. Luong and J. Seppälä, *Eur. Polym. J.*, 2014, **56**, 105-117.

10 M. G. Albu, M. V. Ghica, M. Giurginca, V. Trandafir, L. Popa and C. Cotrut, *Rev. Chim. Bucharest*, 2009, **60**, 666-672.

11 W. Qiang, F. Zhang, L. Jie, B. Li and C. Zhao, *Polym. Chem.*, 2010, **1**, 1430-1433.

12 X. Jing, H. Y. Mi, B. N. Napiwocki, X. F. Peng and L. S. Turng, *Carbon*, 2017, **125**, 557-570.

13 L. He, D. E. Fullenkamp, J. G. Rivera and P. B. Messersmith, *Chem. Commun.*, 2011, **47**, 7497-7499.

14 Y. Wang, H. Yu, H. Yang, H. Xiang and X. Zhang, *Macromol. Chem. Phys.*, 2017, **218**, 1700348.

15 SPRINGSTEEN, Greg, WANG and Binghe, *Tetrahedron*, 2002, **58**, 5291-5300.

16 M. Vatankhah-Varnoosfaderani, S. Hashmi, A. Ghavaminejad and F. J. Stadler, *Polym. Chem.*, 2013, **5**, 512-523.

17 Z. Lei, Q. Wang, S. Sun, W. Zhu and P. Wu, *Adv. Mater.*, 2017, **29**, 1700321.

18 W. Tao, Z. Ying, Q. Liu, C. Wen and H. Xu, *Adv. Funct. Mater.*, 2017, **28**, 1705551.

19 W. Xie, J. Duan, H. Wang, J. Li, R. Liu, B. Yu, S. Liu and J. Zhou, *J. Mater. Chem. A*, 2018, **6**, 24114-24119.

20 Q. Zhang, X. Liu, L. Duan and G. Gao, *Chem. Eng. J.*, 2019, **365**, 10-19.

21 Y. Zhao, Z. Li, S. Song, K. Yang, H. Liu, Z. Yang, J. Wang, B. Yang and Q. Lin, *Adv. Funct. Mater.*, 2019, 1901474.

22 G. Ge, W. Yuan, W. Zhao, Y. Lu, Y. Zhang, W. Wang, P. Chen, W. Huang, W. Si and X. Dong, *J. Mater. Chem. A*, 2019, **7**, 5949-5956.

23 Y. Xia, Y. Wu, T. Yu, S. Xue, M. Guo, J.-L. Li and Z. Li, *ACS Appl. Mater. Interfaces*, 2019, 11, 21117-21125.

24 H. Chen, X. Ren and G. Gao, *ACS Appl. Mater. Interfaces*, 2019, **11**, 28336-28344.

25 N. Yang, P. Qi, J. Ren, H. Yu, S.-X. Liu, J. Li, W. Chen, D. L. Kaplan and S. Ling, *ACS Appl. Mater. Interfaces*, 2019, **11**, 23632-23638.

26 R. An, B. Zhang, L. Han, X. Wang, Y. Zhang, L. Shi and R. Ran, *J. Mater. Sci.*, 2019, **54**, 8515-8530.

27 X. Zhang, N. Sheng, L. Wang, Y. Tan, C. Liu, Y. Xia, Z. Nie and K. Sui, *Mater. Horiz.*, 2019, **6**, 326-333.

28 Y. Wang, Q. Chang, R. Zhan, K. Xu, Y. Wang, X. Zhang, B. Li, G. Luo, M. Xing and W. Zhong, *J. Mater. Chem. A*, 2019.

29 S. H. Kim, S. Jung, I. S. Yoon, C. Lee, Y. Oh and J. M. Hong, *Adv. Mater.*, 2018, **30**, 1800109.

30 M. A. Darabi, A. Khosrozadeh, R. Mbeleck, Y. Liu, Q. Chang, J. Jiang, J. Cai, Q. Wang, G. Luo and M. Xing, *Adv. Mater.*, 2017, **29**, 1700533.

31 B. Ryplida, K. D. Lee, I. In and S. Y. Park, *Adv. Funct. Mater.*, 2019, 1903209